A CFD study: Influence of biofouling on a full-scale submarine

Dogancan Uzun*, Savas Sezen, Refik Ozyurt, Mehmet Atlar, Osman Turan

Department of Naval Architecture, Ocean and Marine Engineering, University of Strathclyde,100 Montrose Street, Glasgow, G4 0LZ, UK
*corresponding author; e-mail: dogancan.uzun@strath.ac.uk,

ABSTRACT

The aim of this study is to investigate the effect of biofouling related hull roughness on a full-scale submarine by taking into consideration the resistance components, effective power, and nominal wakefield using a Computational Fluid Dynamics (CFD) solver. The validation study was first performed for the model scale submarine form in hydraulically smooth (reference) condition with the available experimental data. Following that, roughness functions, representing the different biofouling conditions, were obtained from the literature and then employed in the wall function of a RANS solver. Later on, the full-scale submarine form was investigated both in the smooth and different grades of biofouling related roughness conditions. The scale effects were examined between the model and full-scale submarine forms through the total resistance components and nominal wake fraction in the smooth reference condition. In rough cases, the frictional resistance values of the full-scale submarine form obtained by RANS solver were compared with those of predicted using Granville`s similarity law analysis based on the flat plate approach. The numerical results showed that the roughness causes a substantial increase in effective power, ranging from ~36% to ~112% depending on the roughness height and submarine speed. Furthermore, with an increasing boundary layer thickness (due to the impact of increasing roughness heights), the mean nominal wake fraction values increase ranging from ~25% to ~68 compared to the reference wake fraction values in the axial direction at the stern.

1 INTRODUCTION

Marine biofouling is the undesired accumulation of waterborne organisms (such as bacteria, algae and barnacles) on wetted surfaces, and it is mainly divided into two major groups as micro and macro fouling. Once a substrate is exposed to seawater, the biofouling process starts immediately from micro-scale to macro-scale in time. Without a doubt, any structure such as ships, offshore structures, buoys, underwater cables and submarines which are in contact with seawater is an object for biofouling [1]

Biofouling causes surface roughness on any submerged surface, severely affecting frictional resistance and thus power requirements. Therefore, biofouling and roughness have been a subject of research for navies and marine industries for a long time. The first study in this area was introduced by William Froude [2] [3] in which plank tests were conducted by towing long and thin plates in a towing tank. The study assumes that the resistance caused by this test structure is due to entirely frictional resistance which is related to the roughness of the surface. By using this indirect method, results can be extrapolated to actual ships through theoretical calculations supported by towing data on ship models or full-scale ships [4]. Following this, comprehensive and systematic towing tests on the Japanese ex-destroyer Yudachi were conducted by Izubuchi [5] in order to show the effect of biofouling on hull resistance. The results showed that the hull resistance is doubled, and the vessel speed reduced to 15.2 knots by losing 4.6 knots at the same engine power after 375 days. In parallel, Davis [6] conducted trial runs on a destroyer at specific periods after it was docked to find the increase in the shaft power due to biofouling accumulation in time. Kempf [7] conducted a series of towing tests with 76.8-meter pontoon under various surface conditions to develop a roughness coefficient which allows calculating the effect of roughness on frictional resistance. Next, Liljegren [8] used the data provided by Kempf [7] and compared the frictional coefficients for varnished and steel surfaces. In McEntee [9], three meter-long and 0.61-meter-wide steel plates were immersed in the Chesapeake Bay, and their frictional resistance was measured periodically by towing at velocities ranging from 2 knots to 9 knots at the United States Experimental Basin. The results showed that the resistance of the plates increased four times compared to clean conditions in a twelve months period.

The studies investigating the effect of biofouling on ships conducted in various ways can be found in the literature. Full-scale ship trials [10] [11], towed flat plates [12] [13], concentric cylinders [14], rotating disks [14] [15], model ship [14], turbulent pipe flow [16], water tunnel [17] [18], flowcell [19] tests can be given as critical examples. Schultz [20] conducted flat plate tests to compare the frictional resistances of fouling release and biocide-based coatings under fouled and clean conditions. The results showed that even soft fouling increased the frictional resistance substantially. Following that, Schultz [21] made predictions on the effect of biofouling on ship frictional resistance and shaft power by following Granville's similarity law scaling [22] [23] for a frigate based on the experimental data given in Schultz [20].

Recently, several studies have focused on the impacts of specific fouler species on the frictional resistance. Demirel et al. [24] conducted flat plate tests by towing flat plates covered with 3D barnacles in varying sizes and coverage areas. The test results were extrapolated for a range of ship lengths operating at varying ship speeds. The study showed that there is an increase in frictional resistance in a range between 23% to 119% for barnacle fouling configurations. Uzun et al. [25] conducted experiments with the mixed barnacle bundles, including three different sized barnacles to simulate a more realistic fouling surface. Moreover, a chaotic settlement pattern was proposed, and the effect of settlement pattern on the frictional resistance was investigated.

As stated in Song et al. [26] the effect of biofouling on the frictional resistance was investigated by means of artificial or idealised surfaces in the studies of Womack et al. [27] and Gowing et al. [28]. Once the roughness function, ΔU^+ of any target surfaces is determined, the frictional drag of any surface with an arbitrary length covered with this specific roughness, can be predicted through similarity law analysis [23]. However, the determination of roughness functions is not an easy task due to mainly two primary reasons. The first reason is that there is no universal roughness function and the other reason is the difficulty in calculating a proper roughness length scale for arbitrary rough surfaces. Therefore, the roughness function needs to be determined experimentally for the surface in question [29] [30].

Determination of ΔU^+ can be performed via a direct method, in which the roughness function is directly measured using the mean velocity profile in the log-law region [31] or via indirect methods, i.e. by measuring pressure drop in pipe flow or channel flow [32] or the total drag of flat plates [22] and the torque on rotating disks [33]. Schultz and Myers [30] indicated that the results of indirect methods and direct method showed a good agreement between each other. Moreover, the study showed that the utility of the indirect methods in roughness function determination is relatively cost-effective compared to the direct method. Extensive details on the drag characterisation methods can be found in the review of Yeginbayeva et al., [34]. The obtained roughness functions can then be employed in Granville's similarity law scaling to predict the effect of roughness on the frictional resistance of flat plates of ship length. The further details and examples of the scaling procedure can be found in [20], [21], [35], [36], [24], [37], and [25]. Although Granville's similarity law scaling is an efficient method to predict the effect of roughness on full-scale [21], it is a medium-fidelity method since it has restrictions such as incapability of taking form effects into account.

Computational Fluid Dynamics (CFD) has been widely used as a state-of-the-art method in predicting the effect of surface roughness on the flow in recent years. Eca and Hoekstra [38] stated that the flow around the full-scale ships could be described by Reynolds number of order 10^8 -10^9. Thus, it can be efficiently modelled with the Reynolds-Averaged Navier-Stokes (RANS) equations with the full resolution of time-averaged near-wall flow without incorporating the wall functions. Although there were studies including numerical methods to investigate the effect of a rough surface on the flow [39], [40], [41], [42], [43], [44] none of them was interested in investigating the roughness effect with RANS. Therefore, Eca and Hoekstra [38] modelled sand-grain roughness in the shear stress transport (SST) of the eddy-viscosity k-ω turbulence model by using three types of implementation. Two of the implementations are about the direct application of the no-slip condition at the wall, whereas the third one is based on Apsley's automatic wall function approach [45]. The results indicated that the numerical behaviour of the three approaches show apparent differences and the accuracies of the three methods depend on the roughness regime related to the roughness height. Khor and Xiao [46] used CFD with standard k-ε turbulence model to investigate the

effect of biofouling and antifouling coatings on the drag and lift coefficients. In their study, relatively simple marine geometries such as NACA 4424 airfoil and Defence Research Establishment Atlantic (DREA) submarine hull were used.

Castro et al. [47] showed the applicability of CFD to predict self-propulsion characteristics of a ship in full scale. The computations were carried out with CFD Ship-Iowa which solves the viscous flow with a free surface using a RANS method with a blended *k*-ω/ *k*-ε turbulence model. The *k*-ω/ *k*-ε based DES model turbulence was used to perform full-scale predictions of propeller open water characteristics. The roughness of the surface was taken into account by using wall functions. The authors stated that the first thing to do is finding a sand-grain equivalent roughness for the surface roughness, which can be measured by hull roughness analyser tool to perform CFD computation with surface roughness.

Demirel et al. [48] developed a CFD model in which a Colebrook type roughness function of Grigson (1992) was employed to predict the effect of antifouling coatings on frictional resistance. The SST *k*-ω turbulence model was used to accomplish the RANS equations. The results of the study agreed well with the experimental data of Schultz [20]. Demirel et al. [49] developed a new roughness function model based on the data of Schultz and Flack [50] and utilised in the wall function of the solver. The effect of a range of representative coating and biofouling conditions on the frictional resistance of a flat plate in the length of KRISO Container Ship (KCS) and on the frictional, residuary, wave, total resistance and effective power of the full-scale KCS, were predicted through fully nonlinear unsteady RANS simulations.

Song et al. [26] investigated the effect of calcareous fouling on the ship hydrodynamic characteristics using CFD based on unsteady RANS with SST *k*-ω turbulence model. The roughness functions of barnacle surfaces (Demirel et al. [24]) were employed in the wall function of the CFD software. The analyses performed for model scale flat plate, full-scale flat plate and full-scale KCS hull. Similar studies focussing on modelling the roughness in CFD can be found in [51, 52],[53],[54] and [55].

Even though an extensive amount of research has been conducted towards getting more in-depth knowledge on predicting the effect of roughness on the ship frictional resistance and powering, to the best of the author's knowledge, there is no study investigating the effect of the roughness on a full-scale submarine by using both CFD and similarity law analysis.

A navy project proposal [56] indicated that biofouling significantly decreases the propulsion plant efficiency, thus operational availability and capability by affecting the submarine hull's hydrodynamic resistance. For this reason, this situation leads to a necessity of significant diver labour with the required underwater operation tools, which causes an increase in the maintenance costs from both workforce and radiological aspects. Although submarine hulls are coated with antifouling coatings, they are not efficient under the idle conditions while submarines are in ports. Therefore, the investigation of the impact of biofouling on resistance and self-propulsion characteristics is becoming appealing. In the past, several submarine-related numerical studies were performed to investigate the resistance, self-propulsion, and manoeuvrability in model scale [57], [58], [59] and [60]. However, to the best of the authors` knowledge, there are no specific CFD studies for full-scale submarine simulations both in smooth and rough conditions, in the literature.

For this reason, this paper aims to fill this gap by developing a CFD model to point out the effect of biofouling roughness on resistance, nominal wake and hydrodynamic characteristics of the full-scale submarine form by utilising a roughness function model. This will be achieved by employing the roughness functions proposed in the Uzun et al. [25] into the wall function of the CFD software package STAR-CCM +. It is of note that, these are relatively new roughness functions and it is the first time to be used in the CFD simulations. Following this, Granville's similarity law analysis is carried out for each speed in question to compare the results from CFD.

In this study, CFD analysis was first performed for the model scale submarine form, and results were validated with the experimental data in smooth condition. The simulations were then carried out for the full-scale submarine form to investigate the scale effects in terms of resistance components and nominal wake fraction in smooth conditions. Finally, the roughness function model was utilised in the wall function of CFD software and simulations were performed for six different roughness cases at five different ship speeds ranging from 10 knots to 29 knots. The increases in the frictional resistance due to roughness conditions were predicted and compared with Granville's similarity law analysis results. The effect of roughness on viscous pressure resistance, effective power and nominal wake characteristics was also investigated.

Following this introductory section, the rest of the paper presents the theoretical background behind the computational analyses and the roughness functions, in Section 2. This is followed by numerical modelling, including submarine geometry, computational domain, boundary conditions, and grid structure in Section 3. Next, uncertainty analysis is performed for the numerical set up while validation of the analysis is performed by comparing the model-scale CFD results with the results obtained from the experiment in Section 4. Finally, the results are discussed in detail in Section 5, and further remarks and conclusions are given in Section 6.

2 THEORETICAL BACKGROUND

2.1 *Governing Equations*

The simulations were conducted within the facilities of commercial CFD solver, Star CCM+. The computational fluid dynamics method is based on the discretisation of the Navier-Stokes equations. The governing equations (i.e. continuity and momentum equations) can be written in generalised tensor form, respectively as follows;

$$\frac{\partial(\rho\bar{u}_i)}{\partial x_i} = 0 \tag{1}$$

$$\frac{\partial(\rho\bar{u}_i)}{\partial t} + \frac{\partial\left(\rho\bar{u}_i\bar{u}_j + \rho\overline{u_i'u_j'}\right)}{\partial x_j} = -\frac{\partial\bar{p}}{\partial x_i} + \frac{\partial\bar{\tau}_{ij}}{\partial x_j} \tag{2}$$

Here, $\rho\overline{u_i'u_j'}$ denotes the Reynolds stresses, $\bar{u}$ denotes the mean velocity vector u' denotes the fluctuating velocity vector, $\bar{p}$ denotes the mean pressure, ρ denotes the density and $\bar{\tau}_{ij}$ denotes the mean viscous stress tensor components.

$$\bar{\tau}_{ij} = \mu\left(\frac{\partial\bar{u}_i}{\partial x_j} + \frac{\partial\bar{u}_j}{\partial x_i}\right) \tag{3}$$

where μ is dynamic viscosity.

It should be noted that the simulations were conducted in a steady manner since the submarine model is fully submerged and free surface effects are not present. Thus, the first term of the momentum equation was ignored.

The shear stress transport (SST) k-ω turbulence model was selected for the analyses. The k-ω SST behaves like the standard k-ω model in the near-wall region and gradually blends into the standard k-ε model away from the wall through a blending function. In this way, the free stream sensitivity problem of standard k-ω is eliminated without sacrificing the near-wall performance of the k-ω model. The model is suitable for complex boundary layer flows under adverse pressure gradient and separation. The all y+ formulation was selected to switch automatically between low and high Reynolds wall models for the flow fields with a different boundary layer thickness (hull of the submarine and its appendages).

The commercial CFD solver is based on the finite volume method to discretise the RANS equations. In the numerical approach, the segregated model was used in the solver, and convection terms were discretised using the second-order upwind scheme to increase the accuracy of the solution. The continuity and momentum equations were linked via a predictor-corrector SIMPLE-type algorithm.

2.2 *Roughness and Turbulent Boundary Layer*

Surface roughness increases the turbulence in the boundary layer, which leads an increase in turbulent stress, wall shear stress and skin friction. The velocity distribution in the log-law region can be described by Eq. 4.

$$U^+ = \frac{1}{\kappa}\ln(y^+) + B - \Delta U^+ \quad (4)$$

where $U^+$is the non-dimensional velocity, κ is the von Karman constant, $y^+$is the non-dimensional normal distance from the boundary, B is the smooth log law intercept. Roughness causes a downward shift in the velocity profile, which is commonly shown as ΔU^+, as shown in Figure 1 [61].

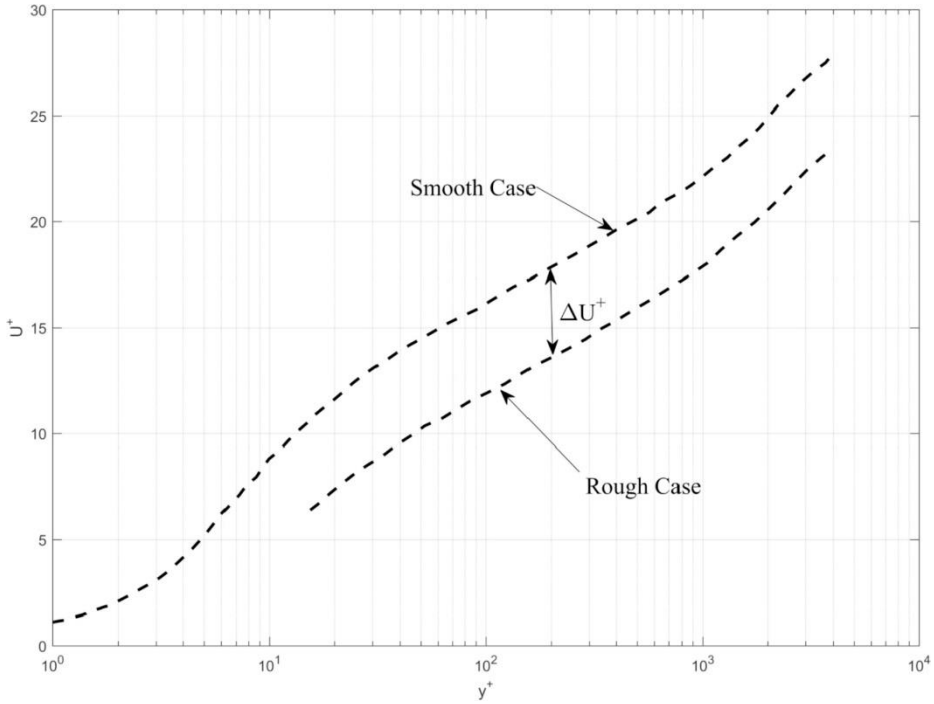

Figure 1 Illustration of a downward shift in log law velocity profile due to the roughness effect (redrawn Schultz and Swain [61])

The roughness function can be written as a function of the roughness Reynolds number, k^+as given in Eq. 5.

$$k^+ = \frac{kU_\tau}{v} \quad (5)$$

where, $U_\tau$is the friction velocity, k is the roughness length scale, and v is the kinematic viscosity. It is important to note that for the smooth conditions $\Delta U^+ = 0$ and roughness functions for the rough cases need to be obtained experimentally.

2.3 *Derivation of Roughness Functions*

First, ΔU^+ and corresponding k^+ values provided in Uzun et al.[25] in which flat plates covered with 3D barnacles were tested in a towing tank, were utilised in the wall function of the CFD software. After that, full-scale CFD simulations were performed based on the modified wall function of CFD model to predict the effect of barnacle roughness on the submarine form, including its appendages. Frictional resistance coefficients of the submarine hull were predicted by using both CFD and Granville's similarity law scaling under the rough conditions. Results were compared with each other, and the improvements of the CFD method over the boundary layer similarity law analysis were pointed out. The effect of roughness on

the different resistance components, pressure distributions over the submarine hull, and wake were investigated.

Uzun et al. [25] conducted an extensive series of towing tank tests of flat plates covered with 3D printed artificial barnacle tiles varying in barnacle sizes, coverage areas and settlement patterns. Roughness functions were then calculated based on the overall method [22], and full-scale predictions were made using boundary layer similarity law analysis [23]. It is of note that the roughness functions and corresponding roughness Reynolds heights which are given in Uzun et al.[25], shows an excellent agreement with the roughness function of Grigson [29], given by $\Delta U^+ = 1/\kappa(1 + k^+)$.

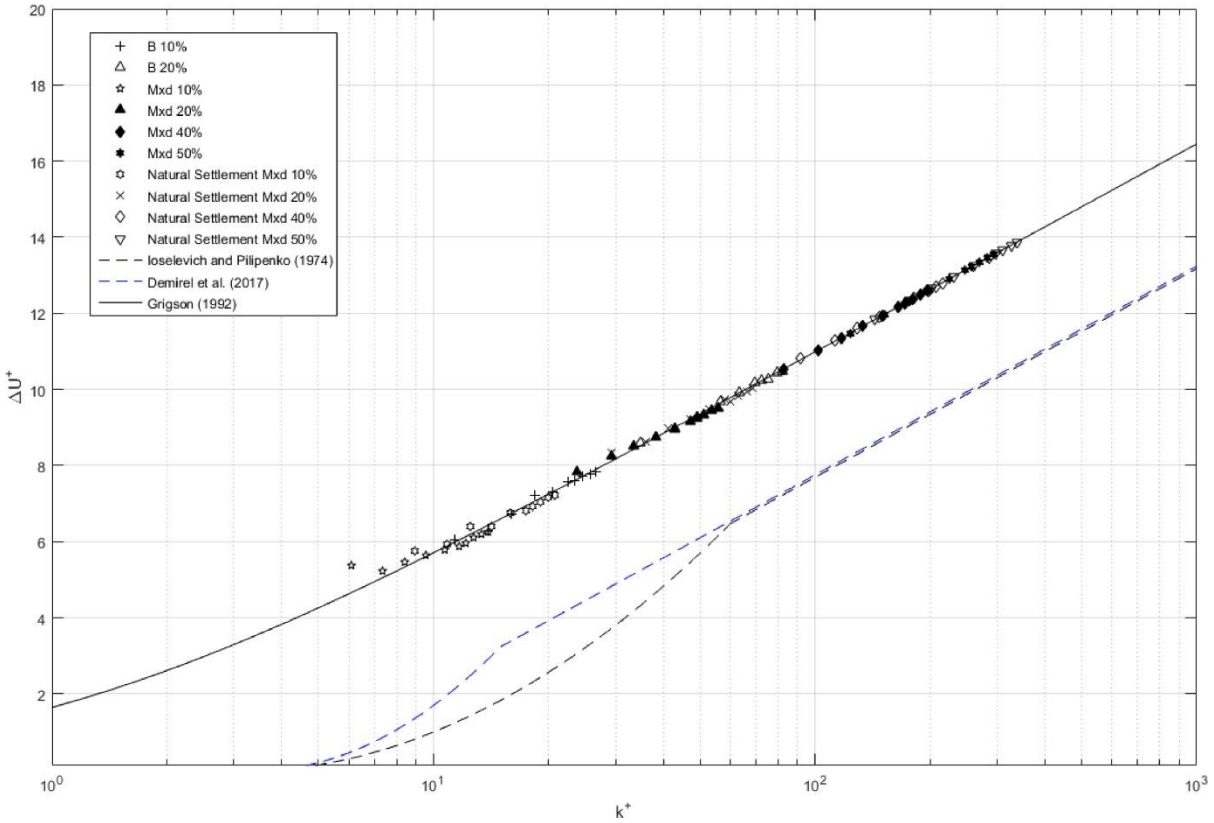

Figure 2 Roughness functions for the test surfaces, adapted from Uzun et al.[25].

In this study, the roughness functions provided in [25] were utilised within the wall function of the CFD model to simulate the rough condition and make full-scale resistance and power predictions for the submarine form.

Table 1 tabulates the roughness length scales of the rough surfaces and Figure 2 illustrates the roughness functions along with the proposed roughness functions of Grigson [29], Ioselevich and Pilipenko [62] and Demirel et al. [24]. Further details on the roughness functions and the experiment can be found in Uzun et al. [25].

Table 1 Roughness length scales of test surfaces, adapted from [25].

Test Surfaces	Surface Coverage (%)	Barnacle Height *h* (mm)	Representative roughness height k_G (μm)
Mix	10	5, 2.5, 1.25	94
Mix	20	5, 2.5, 1.25	337
Mix	40	5, 2.5, 1.25	1056
NS Mix	10	5, 2.5, 1.25	136
NS Mix	20	5, 2.5, 1.25	408
NS Mix	40	5, 2.5, 1.25	1152

3 NUMERICAL MODELLING

3.1 *Submarine Geometry*

The benchmark submarine model, introduced by the Defence Advanced Research Projects Agency (DARPA), has been widely used in the literature for hydrodynamic investigations. The benchmark submarine hull form has two different configurations as AFF-1 and AFF-8. The AFF-1 hull form does not have any appendage (i.e. bare form), whereas AFF-8 configuration has appendages such as four rudders at the aft of the hull and sail. Within the scope of this research, the appended hull form (i.e. AFF-8) was selected for the numerical simulations. The main geometrical properties of the submarine form and general view are given in Table 2 and Figure 3, respectively. The detailed features of the submarine model can be found in the experimental report of Groves et al. [63].

Table 2 The main properties of the DARPA Suboff Form [63].

	AFF-8 (Model Scale, λ =24)	**AFF-8 (Full Scale, λ =1)**
L_{OA} (m)	4.356	104.544
L_{BP} (m)	4.261	102.264
D_{max} (m)	0.508	12.192
S (m^2)	6.348	3656.48
∇ (m^3)	0.706	9759.744

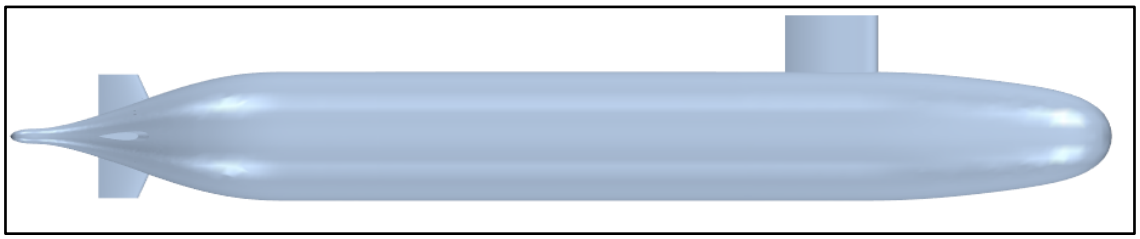

Figure 3 The general views of the submarine form with appendages.

3.2 *Computational Domain and Boundary Conditions*

The rectangular computational domain was selected to solve the flow around the submarine forms for both model and full scale. The domain lengths of up and downstream of the hull were set the length of $1.5L_{BP}$ and $5L_{BP}$, respectively. Upper and bottom sides of

the domain were extended to $2L_{BP}$ from the centre of the submarine hull. It should be noted that the selected domain dimensions satisfy the recommendations of ITTC [64].

The initial and boundary conditions should be defined in accordance with the numerical problem to provide the well-posedness of the solution, which depends on the choice of boundary conditions. Selecting suitable boundary conditions is vital for accurate numerical modelling [65]. The computational domain and boundary conditions are illustrated in Figure 4.

The negative 'X' direction was identified as velocity inlet, whereas the positive 'X' side was defined as pressure outlet. The remaining surfaces were identified as symmetry planes. The submarine hull with appendages was defined as a wall with the no-slip condition to satisfy the kinematic boundary condition.

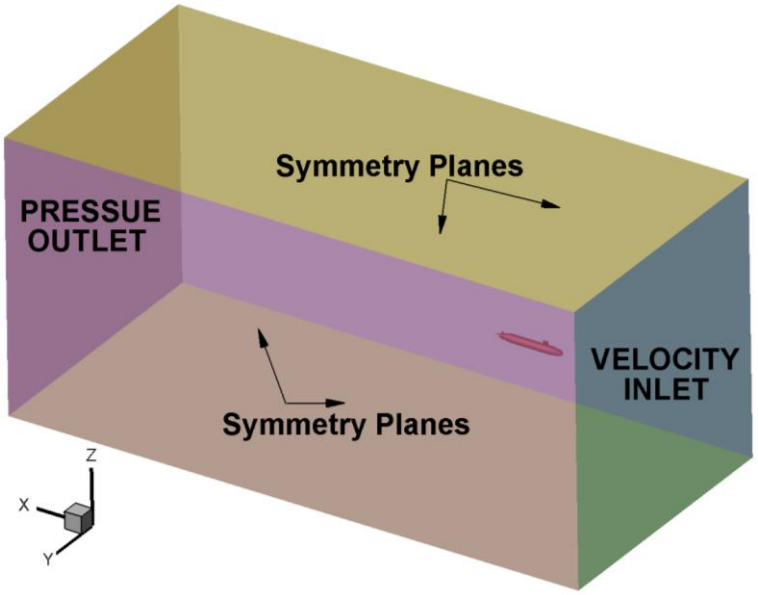

Figure 4 The representative of the computational domain and boundary conditions.

3.3 *Grid Structure*

The adaptation of the suitable grid structure can be considered one of the challenges in the most hydrodynamic applications, closely linked to the discretisation errors in the numerical solvers. In order to eliminate the discretisation errors, the suitable grid structure should be used in the numerical solvers. In this study, the region-based mesh topology was used to discretise the computational domain with finite volume method within the facilities of Star CCM+ solver. The trimmer mesh with hexahedral elements was adopted to increase the accuracy of the solution with optimum element count. The additional mesh refinements were then employed around the hull and appendages to solve the flow field properly. The unstructured mesh structure around the submarine form can be seen in Figure 5.

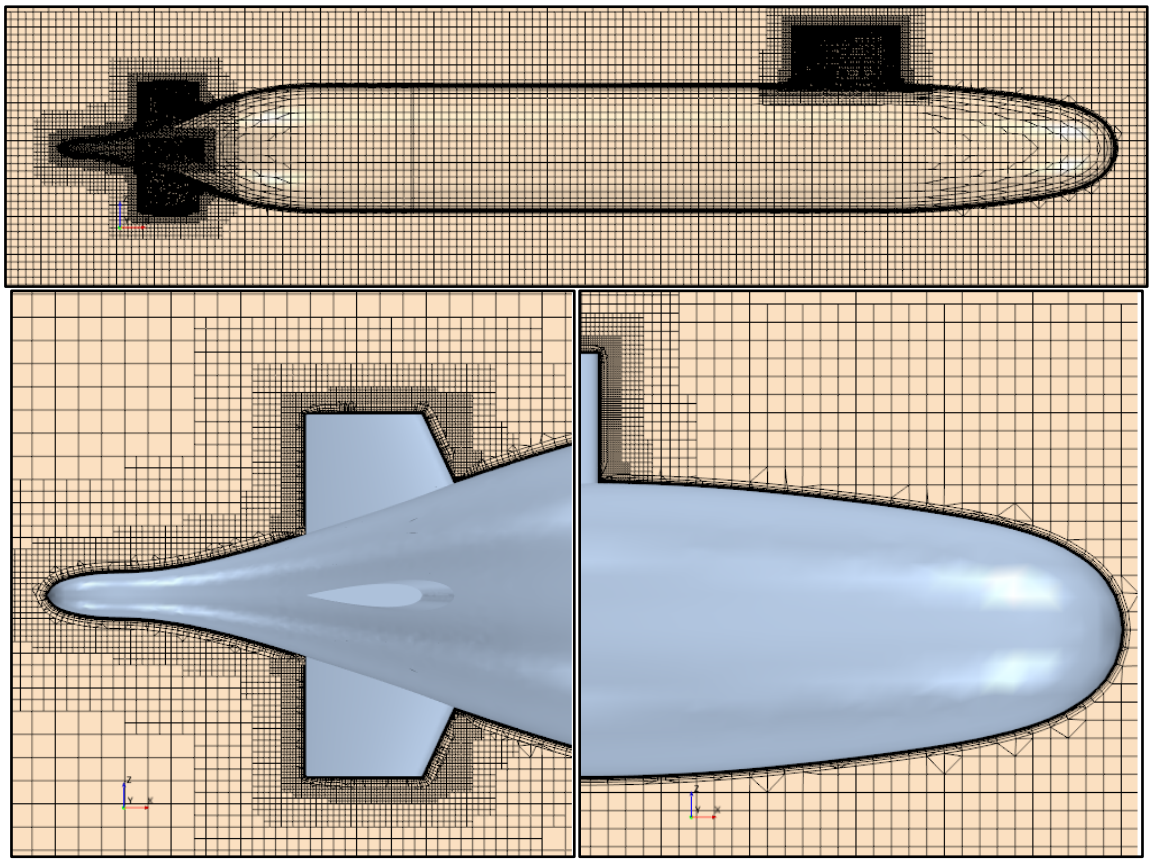

Figure 5 Unstructured grid around the full-scale submarine form

It should be noted that the value of y^+ was selected higher than 30 as placing y^+in the buffer layer region ($5<y^+<30$) can lead large numbers of errors since the blending/switching behaviour is inaccurate for the wall function approach in this region. Moreover, y^+should also be higher than k^+values, as recommended by Star CCM+ to impose the effects of roughness functions. In other words, the distance of the first grid node to the wall must exceed the roughness size; otherwise, the skin friction coefficient is under-predicted.

4 VERIFICATION AND VALIDATION

4.1 *Verification Study*

The verification study was conducted to determine the uncertainty level of the numerical study and sufficient grid spacing for the numerical simulations. The Grid Convergence Index (GCI) method, which is based on the Richardson extrapolation, was used to predict the uncertainty of the solution. The uncertainty method (i.e. GCI) was recommended for CFD verification studies in the ITTC procedure [64]. This method was first proposed by Roache [66] and has employed in many studies in the literature. In this study, the methodology described by Celik et al. [67] was applied. The detailed procedure of the method can be found in the study of Celik et al. [67].

The refinement factor (r) was selected as $2^{0.5}$, which is generally employed in CFD applications. Besides, it is recommended to use the refinement factor greater than 1.3. In this method, three different solutions are desired to accurately assess the uncertainty level of the numerical solution [68]. Thus, the three solutions were utilised in this study.

The difference between the solution scalars (ε) can be found using the following equation,

$$\varepsilon_{21} = \varphi_2 - \varphi_1, \quad \varepsilon_{32} = \varphi_3 - \varphi_2, \tag{6}$$

Here, $\varphi_1, \varphi_2, \varphi_3$ indicates the fine, medium and coarse grid solution, respectively. It is to be noted that the total elements are around 0.98×10^6, 0.56×10^6 and 0.37×10^6 in model scale for fine, medium and coarse grid structures, whereas these numbers altered to 1.2×10^6, 0.76×10^6 and 0.47×10^6 for fine, medium and coarse grid structures, respectively for full-scale simulations. The solution scalar was selected total resistance value both in the model and full-scale simulations at V_M=3.051 m/s and V_S=14.95 m/s, respectively.

Convergence conditions of the numerical solution can be calculated as follows,

$$R = \frac{\varepsilon_{21}}{\varepsilon_{32}} \tag{7}$$

The determination of the solution can be assessed according to the range of R values [69]. Oscillatory convergence: -1 < R < 0, monotonic convergence: 0 < R < 1, oscillatory divergence: R < -1 and monotonic divergence: R > 1.

The extrapolated value can be calculated using the following equation,

$$\varphi_{ext}{}^{21} = (r^p\varphi_1 - \varphi_2)/(r^p - 1) \tag{8}$$

The approximate and extrapolated relative errors are defined as follows,

$$e_a{}^{21} = \left|\frac{\varphi_1 - \varphi_2}{\varphi_1}\right| \quad e_{ext}{}^{21} = \frac{|\varphi_{ext}{}^{12} - \varphi_1|}{\varphi_{ext}{}^{12}} \tag{9}$$

Finally, the uncertainty level of the numerical solution can be calculated by,

$$GCI_{fine}{}^{21} = \frac{1.25e_a{}^{21}}{r_{21}{}^p - 1} \tag{10}$$

Here p is the apparent order of the method. The element count and solution of the scalars for each grid structures and the uncertainty level of the numerical study for both model and full-scale submarine forms are given in Table 3 and 4, respectively.

Table 3 Spatial Converge study results at model scale submarine form (V_M =3.051 m/s)

N_1	982300
N_2	564431
N_3	367968
φ_1	98.987
φ_2	100.969
φ_3	104.521
r_{21}	1.202
r_{32}	1.153
ε_{21}	1.982
ε_{32}	3.552
p	3.945
q	0.280
s	1
${e_a}^{21}$	0.020
${e_{ext}}^{21}$	0.019
${\varphi_{ext}}^{21}$	97.139
GCI_{FINE} (%)	2.334

Table 4 Spatial Converge study results at the full-scale submarine form (V_S =14.95 m/s)

N_1	1270488
N_2	767315
N_3	474216
φ_1	1.970E-3
φ_2	1.996E-3
φ_3	2.087E-3
r_{21}	1.183
r_{32}	1.174
ε_{21}	2.625E-5
ε_{32}	9.205E-5
p	7.422
q	0.051
s	1
${e_a}^{21}$	0.013
${e_{ext}}^{21}$	5.395E-3
${\varphi_{ext}}^{21}$	1.960E-3
GCI_{FINE} (%)	0.671

As a result of the uncertainty study, the fine mesh was selected both for model and full-scale simulations. It should be noted that the number and thickness of the prism layer were set according to the maximum roughness height given in Table 1. As a result of the uncertainty study, the same properties of near-wall mesh (i.e. number and thickness of the prism layer) were not changed for each velocity and roughness type due to the computational cost as there are several velocities and roughness heights investigated in the scope of this study.

4.2 *Validation Study*

Following the verification study, the numerical results of the total resistance in the smooth case for model scale submarine form were validated with the experimental data. Figure 6 shows that there is a good agreement between numerical and experimental results. The absolute difference in total resistance values between CFD and experiment was calculated to be a maximum of 7%. The numerical results for the full-scale submarine form will be given in the next section. Here λ (Length of ship/Length of model=24) is the scale ratio.

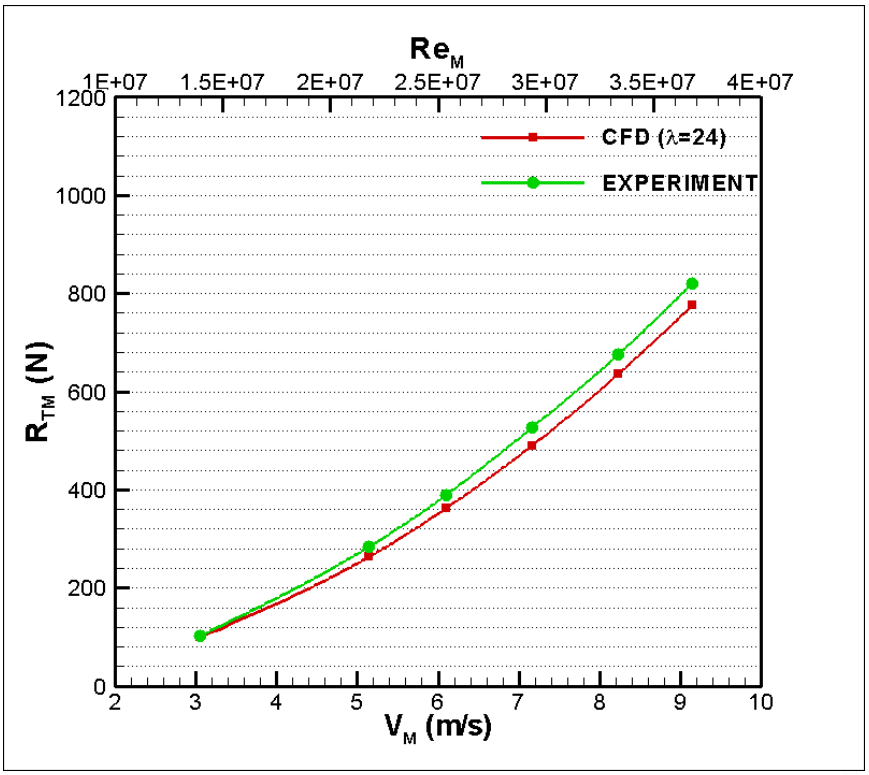

Figure 6 Validation of resistance values for model scale submarine form (λ=24)

5 NUMERICAL RESULTS

5.1 *The comparison of resistance and its components between model and full scale in the smooth case*

The total resistance of the vessel (R_T) is mainly comprised of two components; the frictional resistance (R_F) and residuary resistance (R_R) which can be written as follows;

$$R_T = R_F + R_R \tag{9}$$

where R_R is the summation of the wave-making resistance (R_W) and viscous pressure resistance (R_{VP}), and it is originated from the drag related normal pressure while R_F is due to the friction between the hull and fluid.

$$R_R = R_{VP} + R_W \tag{10}$$

The total resistance and its components are generally identified in non-dimensional form by dividing each term by the object's wetted surface area and dynamic pressure. The residuary resistance component can be considered a function of Froude number (*Fn*) whereas the frictional resistance component is a function of Reynolds number (*Re*). The non-dimensional form of resistance components can be written as follows,

$$C_T = C_F(Re) + C_R(Fn) \tag{12}$$

The frictional resistance component can be calculated by using the ITTC-1957 extrapolation formula as follows [64],

$$C_F = \frac{0.075}{(\log(Re) - 2)^2} \tag{13}$$

It should be born in mind that in this study, the submarine form is fully submerged. Thus, there is no wave resistance component, and the residuary resistance is only composed of viscous pressure resistance (R_{VP}) which occurs due to separation and energy loss created by eddy motions. R_{VP} generally constitutes a small portion of residuary resistance in comparison to R_W for a ship in the free surface. Additionally, the Reynolds and Froude number can be given, respectively, as follows,

$$Re = \frac{VL}{v} \tag{14}$$

$$Fn = \frac{V}{\sqrt{gL}} \tag{15}$$

Here, V is the ship velocity (m/s), L is the ship length (m), g is the acceleration of gravity (m/s^2), and v is the kinematic viscosity of the fluid (m^2/s). *Fn* similarity is satisfied between model and full scales for free-surface vessels (i.e. ship case). In contrast, *Re* similarity is preferred for submerged bodies since there will be no free surface effect. *Re* and *Fn* similarity can be written between model and full scale, respectively.

$$\frac{V_M L_M}{\vartheta_M} = \frac{V_S L_S}{\vartheta_S} \rightarrow V_S = \frac{V_m}{\lambda} \tag{16}$$

$$\frac{V_S}{\sqrt{g_S L_S}} = \frac{V_M}{\sqrt{g_M L_M}} \rightarrow V_S = V_M \sqrt{\lambda} \tag{17}$$

As can be seen in Eq. 16, if the *Re* similarity is satisfied between the model and full scale, the model-scale velocities exceed the practical speed limitations of experimental facilities. The model-scale submarine tests were conducted at five different velocities (i.e. between 3.051 and 9.152 m/s) in the David Taylor Model Basin (Groves et al., 1989). Although the *Re* similarity is likely to be used for fully submerged bodies, in our case, the full-scale velocities become unrealistic with *Re* similarity. For this reason, *Fn* similarity is deemed to be more applicable to find the full-scale velocities. However, even if *Fn* similarity is satisfied, the full-scale submarine velocities still remain in an unrealistic speed range. In our study, the velocities obtained by *Fn* similarity were used to investigate the scale effects between model and full-scale submarine forms in smooth condition. Nevertheless, more realistic submarine

velocities were selected between 10 knots and 29 knots (i.e. 10, 15, 20 and 25 knots) to investigate the effects of roughness on submarine hydrodynamic performance. Table 5 tabulated the full-scale velocities obtained by both *Re* and *Fn* similarities.

Table 5 The full-scale velocities obtained by *Re* and *Fn* similarities

V_M (m/s)	V_S (m/s) (*Re* Similarity)	V_S (m/s) (*Fn* Similarity)
3.051	0.127	14.947
5.144	0.214	25.200
6. 096	0.254	29.864
7.161	0.298	35.082
8.231	0.348	40.324
9.152	0.381	44.835

Figure 7 shows the numerical frictional resistance results obtained by CFD and ITTC-1957 formulation for full-scale submarine form in smooth condition. In smooth condition, the y^+ values change between 223 and 1730 from 10 knots to 87 knots. As can be seen in Figure 7, there is a good agreement between numerical results and ITTC formulation with a maximum of 3.68% difference.

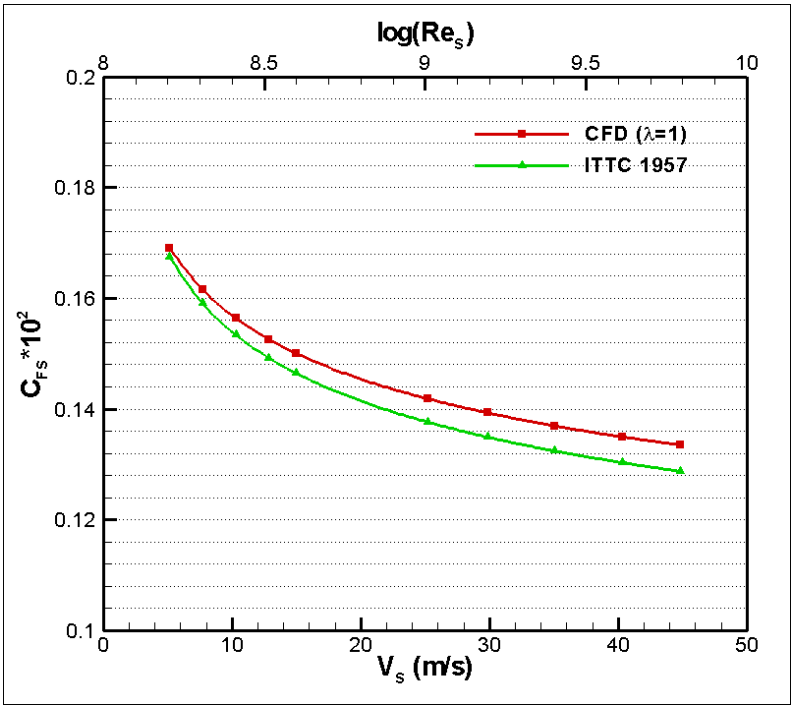

Figure 7 Comparison of frictional resistance component with CFD and ITTC formulation.

The numerical results of the model and full-scale submarine forms were compared through the total resistance and viscous pressure resistance coefficients in the smooth condition in Figure 8. As expected, the total and viscous pressure resistance values decrease with an increase in *Re* numbers. Besides, the magnitudes of the model's total resistance coefficient are

higher than those of the full-scale submarine due to higher frictional resistance and viscous pressure resistance coefficients related to the differences in the boundary layer structure and thickness at different scales.

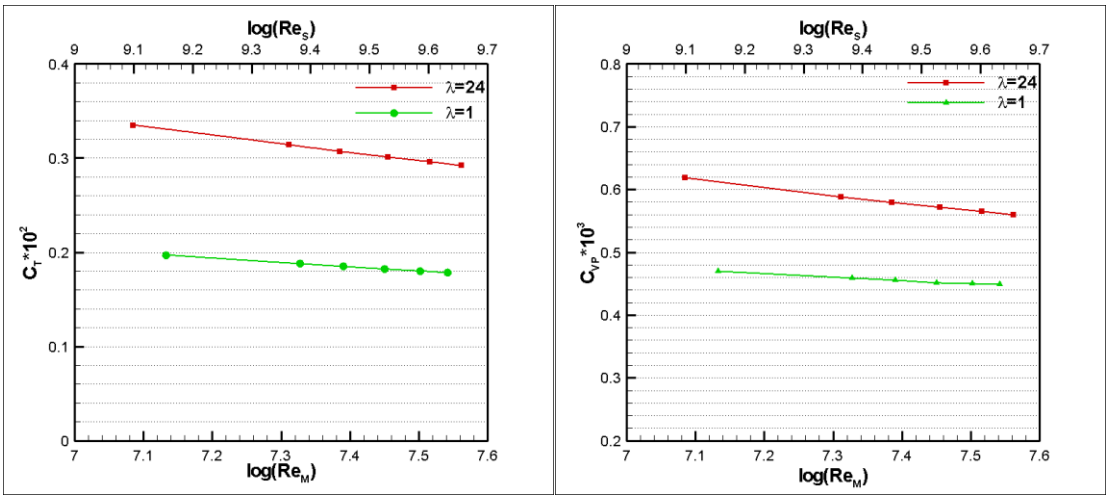

Figure 8 Comparison of total and viscous pressure resistance both for model and full scale in smooth condition.

5.2 *The comparison of nominal wakes between model and full-scale in smooth condition*

The wakefield of a ship occurs due to relative motion between the hull and flow with a free surface. In the classic naval architecture literature, the wakefield can be presented on the propeller plane by using non-dimensional wake fraction (w) parameter, which can be described as the "nominal" and "effective" wake terms depending on the presence of the propeller. While the former is defined in the absence of the propeller, the latter includes the effect of the propeller's action (not the physical presence of the propeller) in the wakefield inflow but excluding the propeller induced velocities. The nominal wake fraction (w), can be divided into three components given by Eq 18; [70]

$$w = w_p + w_f + w_w \tag{18}$$

where w_p is the potential wake fraction, w_f is the frictional wake fraction and w_w, is the wave-induced wake fraction component. The potential wake occurs due to the increase in pressure around the stern stagnation region, whereas the frictional wake arises due to the viscous nature of the fluid passing over the hull and dominates the nominal wakefield. The wave component of the wake is due to the orbital motion of the Kelvin wave profiles [71]. As the *Fn* similarity is satisfied between model and full-scale of the vessel in the model tests, the potential wake fraction can be considered the same for both model and full-scale. However, due to the difference in *Re* numbers between the model and full scale, the boundary layer thickness ratio will be significantly less in full-scale and resulting in the well-known scale effects [72], which still being discussed in the literature [64]. On the other hand, since the submarine hull is fully submerged, the wave-induced component of the wake can be ignored, and the wake fraction mainly composed of the frictional wake component.

Figure 9 shows the location of the predicted nominal wakefields in the numerical calculations for model and full-scale submarine forms (i.e. x/L= 0.978, 1.04, 1.20). The predictions are given in Figure 10 for the non-dimensional axial velocity distributions at three different locations both in the model and full-scale. The reduced axial velocities can easily be seen as the shadowing effects of the appendages on the wakefield contour plots in Figure 10.

The V-shaped carving, which was triggered by the sail, was observed in the numerical solutions, especially at x/L=0.978 (i.e. propeller plane) similar to that observed in Wang et al., 2015. The non-dimensional axial velocity contours at the different planes manifest themselves as the higher wake velocities and hence lower nominal wake fraction in full-scale due to the scale-effect associated with the *Re* number and boundary layer thickness ratio. It should be noted that the propeller diameter D_M and hub to dimeter ratio (D_{hub}/D) was set to 0.262 m and 0.226, respectively [60].

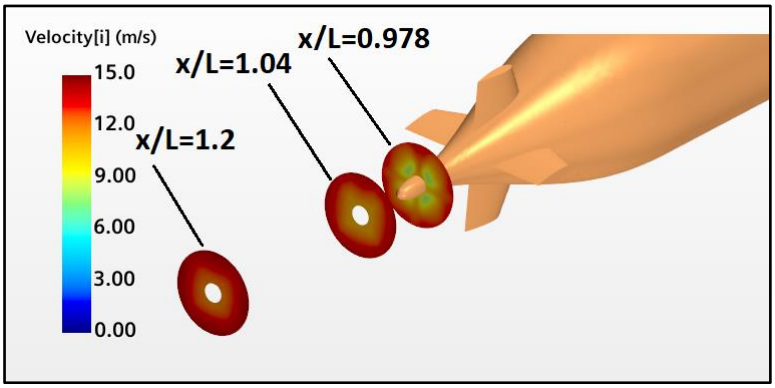

Figure 9 Representation of measured nominal wakefields location both in the model and the full-scale (smooth conditions)

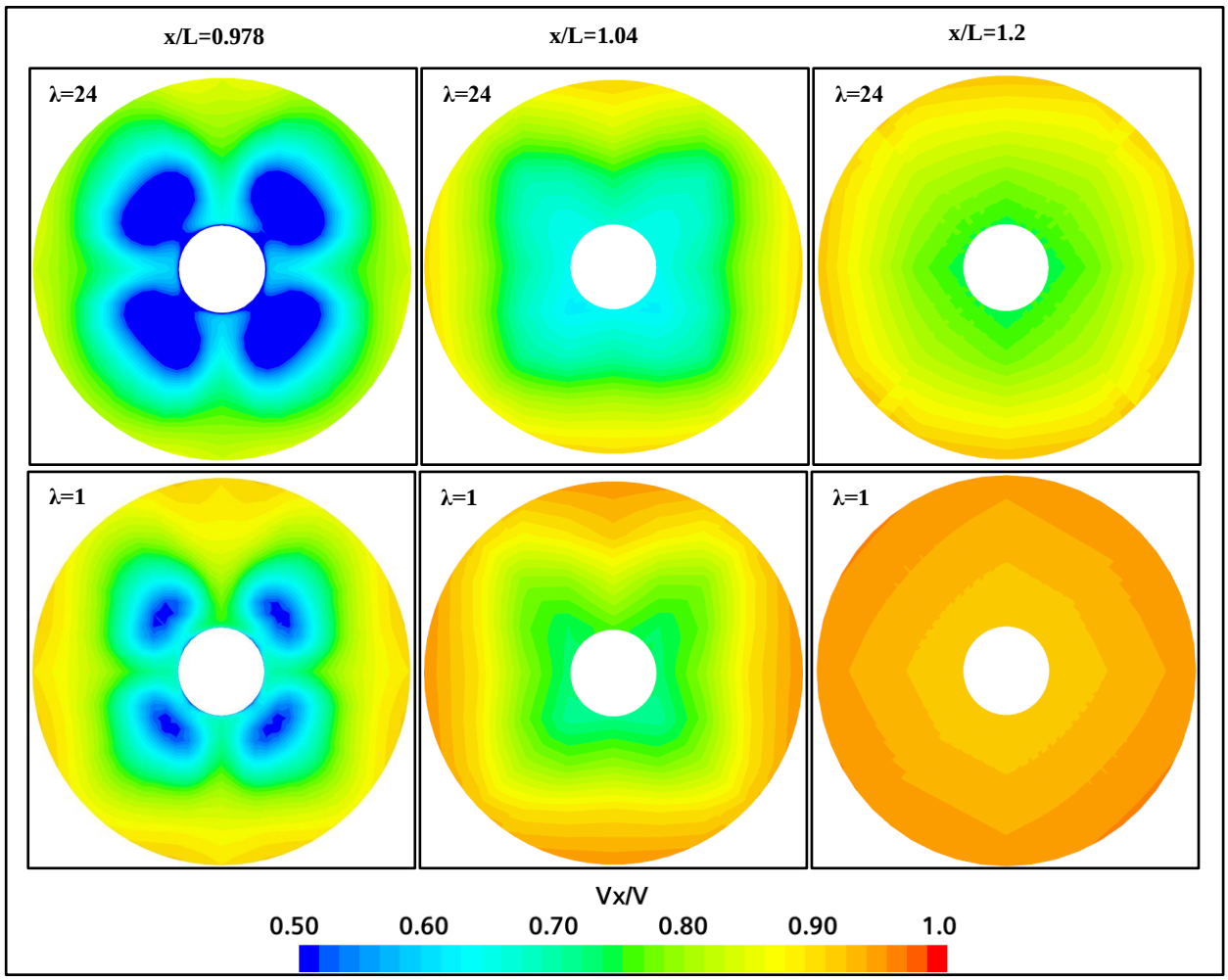

Figure 10 The non-dimensional axial velocity distributions at three different locations for model and full scale in smooth conditions ($\boldsymbol{V_M}$=3.051 m/s and $\boldsymbol{V_S}$=14.95 m/s)

The mean value of the nominal wake fraction at the propeller plane can be calculated by integrating the wakefield as follows;

$$\bar{W}_T = \frac{\int_{r_h}^{R} r \int_0^{2\pi} w_T \, d\emptyset \, dr}{\pi(R^2 - {r_h}^2)} \tag{19}$$

Here, w_T is the Taylor wake fraction, R is the propeller diameter and r_h, is the hub diameter. The calculated wake fractions for different axial velocities at x/L=0.978 (i.e. the propeller plane) for both model and full-scale submarines in the smooth condition are shown in Figure 11. It can be seen in this figure that the nominal wake fraction values decrease with an increase in *Re* number as well as with the reduced scale ratio. The slope of the wake fraction lines also decreases with an increase in *Re* number.

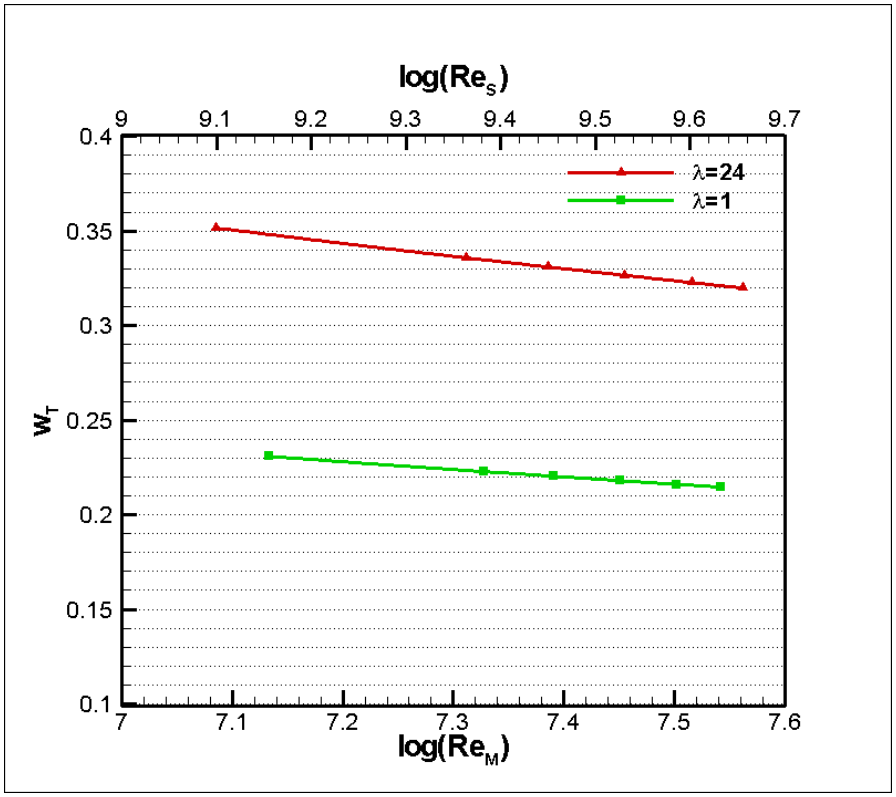

Figure 11 The comparison of nominal wake fractions for both model and full-scale submarine forms in smooth condition (x/L=0.978)

5.3 *The effect of roughness on the hydrodynamic characteristics of the submarine in full-scale*

In the previous section, the model and full-scale submarine forms were compared in terms of the resistance components and wakefields in the smooth condition. In this section, a CFD model with modified wall function approach was developed to investigate the effects of roughness on resistance, effective power, as well as wakefields for the full-scale submarine in a velocity range from 10 knots to 29 knots. The details of the roughness functions are tabulated in Table 2. Figure 12 illustrates the predicted wall shear stresses on the submarine hulls both in the smooth and rough conditions. As expected, the roughness triggers and increase the wall-shear stress dramatically on the submarine form with appendages.

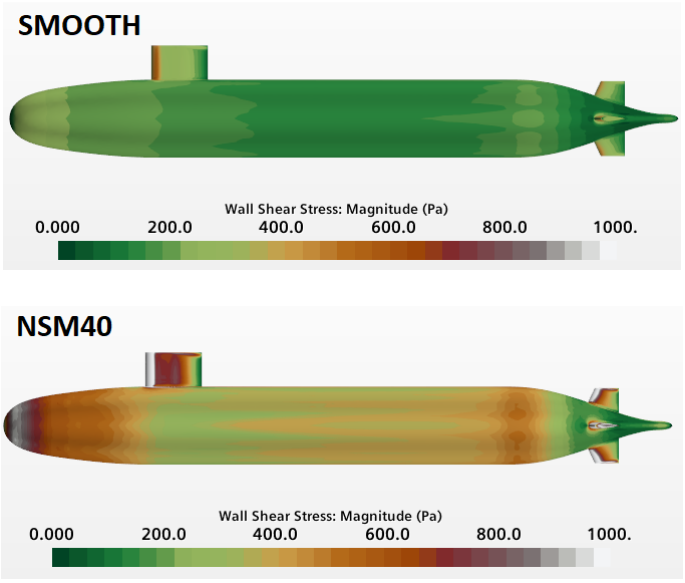

Figure 12 The comparison of the wall shear stress between smooth and rough conditions at 29 knots

As the wall shear stress (or frictional velocity) increases in the rough cases, the non-dimensional y^+values increase inevitably. Figure 13 shows the change in the average y^+values calculated on the submarine hull with respect to the representative roughness height (i.e. k_G). It should be noted that the average y^+values also rise with an increase in submarine velocity.

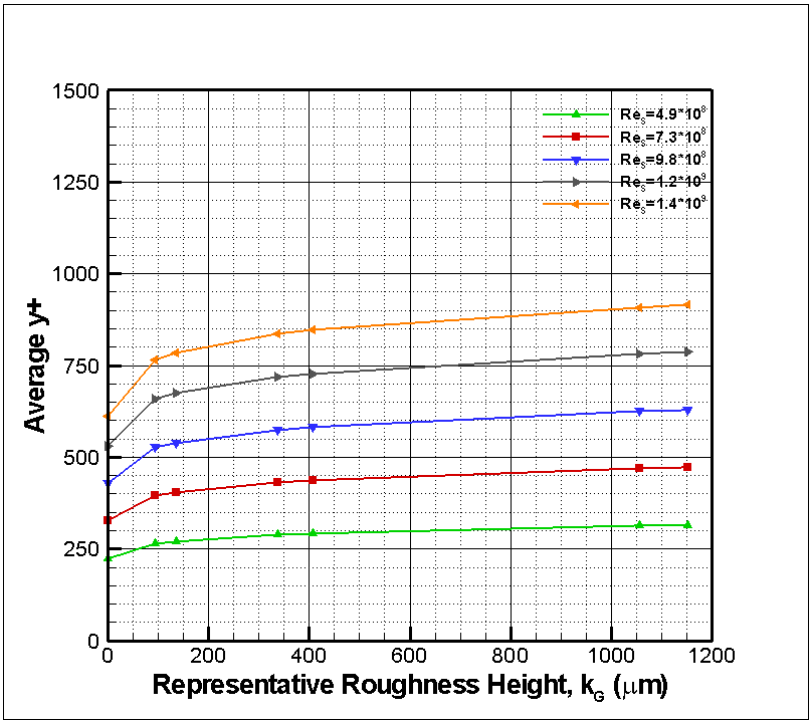

Figure 13 The change of y^+ values with roughness and velocity.

The numerical frictional resistance coefficients (C_F) obtained by CFD were compared with Granville's similarity law scaling method [22], [23]. In the latter method, the submarine geometry is assumed to be replaced by the flat plate with the length of the submarine. Figure 14 shows that there are discrepancies between the percentage increases in C_F values with respect to smooth surface obtained by CFD and Granville`s approach at different velocities. This can be attributed to the fact that the boundary layer becomes strongly thickened due to the backflow close to the wall, so boundary layer mass gets away from the wall. The velocity gradients are perpendicular to the wall, and the wall shear stress ($\tau_w = 0$) vanishes at the separation point. Even the small changes in the shape of the body, particularly where the pressure distribution is strongly affected (i.e. appendages of the submarine), flow separation can occur easily. This could be the reason for the discrepancies between the two approaches as it is not possible to capture this effect in Granville's approach.

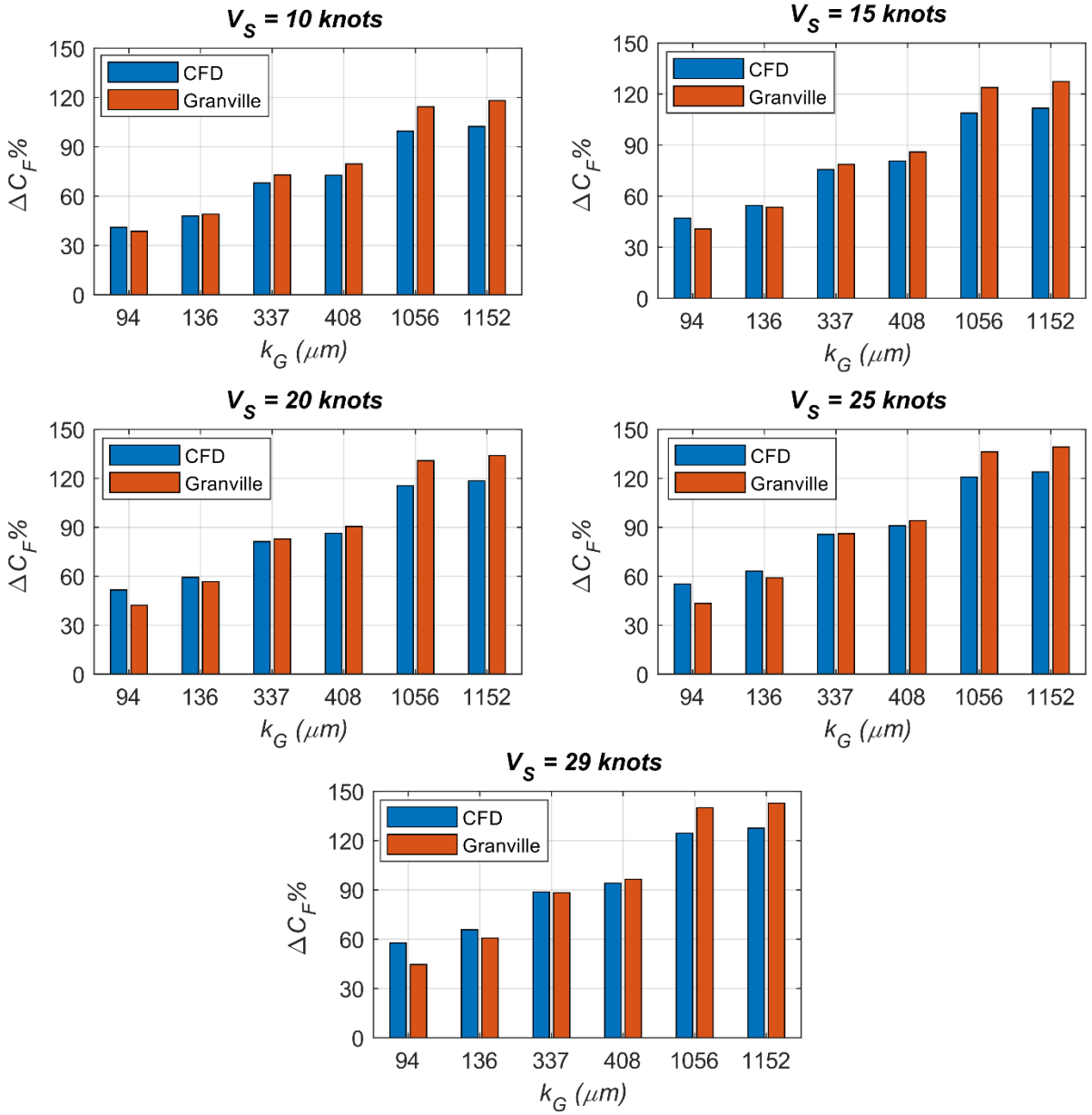

Figure 14 The comparison of C_F values between CFD and Granville`s approach.

Figure 15 illustrates the pressure coefficient (C_P) which is the pressure non-dimensionalised by ρV^2 along the hull for both smooth and rough cases at the top and bottom side of the submarine form. It is important to note that '0' indicates aft of the submarine form, whereas '1' indicates the forward of the submarine. It can be observed that the surface roughness mainly affects the sail and aft region of the submarine with the manifestation of decreasing pressure, while the rest of the hull pressures is not affected significantly. Therefore, as well as the increased frictional drag, the roughness will further increase the viscous pressure component of the submarine hull.

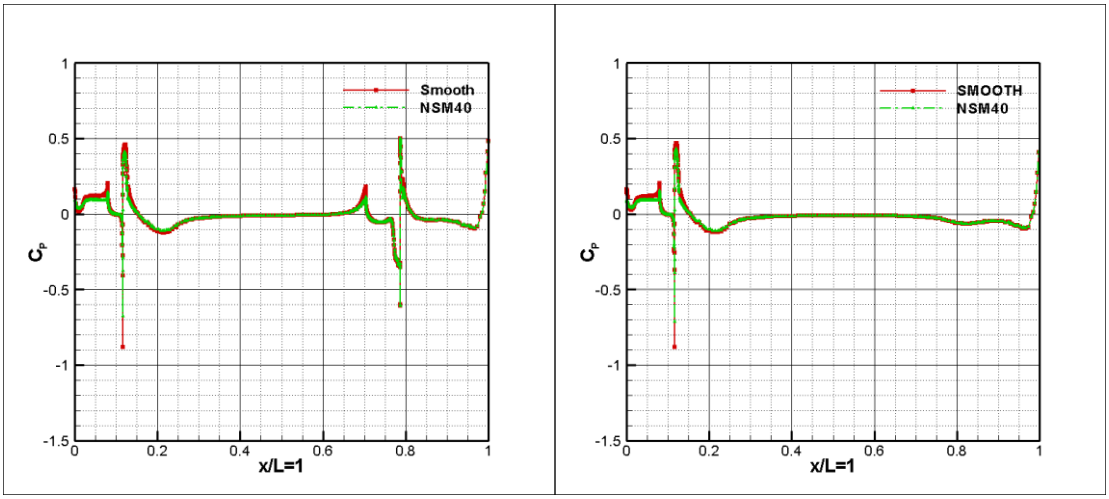

Figure 15 The non-dimensional pressure distributions along with the form at 29 knots (left: top of the form; right: bottom of the form)

Following the C_F values comparison between the CFD and Granville`s approaches, the C_T and C_{VP} values were compared at several velocities for the smooth and rough cases in Table 6. It can be seen from the table, the C_T and C_{VP} values increase at the same *Re* numbers as the roughness height increases.

It should be noted that the values of C_F and C_{VP} remain almost constant at increasing Re numbers under the same surface roughness condition. This can be attributed to the fact that the flow condition is fully-rough as the selected roughness elements penetrate the linear sublayer. When the flow is in the fully rough regime, C_F and C_{VP} values become independent of *Re* numbers, and the surface drag is comprised of the form drag and eddy shedding of the roughness elements. Due to the pressure differences at the aft of the submarine form and the sail, the C_{VP} values increase in the rough cases in comparison to smooth condition.

Table 6 Comparison of resistance components at different speeds

	Re=4.9*10^8 (V_S=10 knot)		*Re*=7.3*10^8 (V_S=15 knots)		*Re*=9.8*10^8 (V_S=20 knots)		*Re*=1.2*10^9 (V_S=25 knots)		*Re*=1.4*10^9 (V_S=29 knots)	
k_G (μm)	C_T	C_{VP}	C_T	C_{VP}	C_T	C_{VP}	C_T	C_{VP}	C_T	C_{VP}
0	2.186E-03	4.958E-04	2.100E-03	4.851E-04	2.042E-03	4.780E-04	1.999E-03	4.729E-04	1.971E-03	4.696E-04
94	2.984E-03	6.007E-04	2.976E-03	5.997E-04	2.971E-03	5.992E-04	2.968E-03	5.988E-04	2.967E-03	5.987E-04
136	3.119E-03	6.184E-04	3.113E-03	6.176E-04	3.109E-03	6.172E-04	3.107E-03	6.170E-04	3.106E-03	6.168E-04
337	3.511E-03	6.713E-04	3.508E-03	6.709E-04	3.506E-03	6.707E-04	3.505E-03	6.706E-04	3.504E-03	6.705E-04
408	3.604E-03	6.840E-04	3.601E-03	6.837E-04	3.599E-03	6.835E-04	3.598E-03	6.834E-04	3.597E-03	6.833E-04
1056	4.129E-03	7.541E-04	4.126E-03	7.539E-04	4.125E-03	7.539E-04	4.124E-03	7.538E-04	4.124E-03	7.537E-04
1152	4.182E-03	7.609E-04	4.180E-03	7.608E-04	4.179E-03	7.607E-04	4.178E-03	7.606E-04	4.177E-03	7.605E-04

5.4 *The effect of roughness on the effective power*

The total resistance coefficients, C_T, were calculated based on the full-scale simulations for smooth and the rough conditions at five different ship speeds. Following this, the percentage increases in the P_E due to roughness were calculated by using Eq. 20.

$$\Delta P_E\% = \frac{C_{TR} - C_{TS}}{C_{TS}} \times 100 \tag{20}$$

Here, C_{TR} is the total resistance coefficient at rough condition, whereas C_{TS} is the total resistance coefficient at the smooth condition. As shown in Figure 16, the roughness conditions cause a substantial increase in P_E values, ranging from ~36% to ~91% at 10 knots and ~50% to ~111% at 29 knots. The figure states that the effect of roughness on P_E increases with the increasing ship speed as expected. The results of this study are in contrast to earlier findings of Song et al. (2019) which showed the effect of roughness on the effective power was higher at 19 knots compared to those at 24 knots for the full-scale KCS hull. This can be attributed to the fact that DARPA form was fully submerged, whereas KCS hull was in interaction with the free surface, which also creates wave-making resistance.

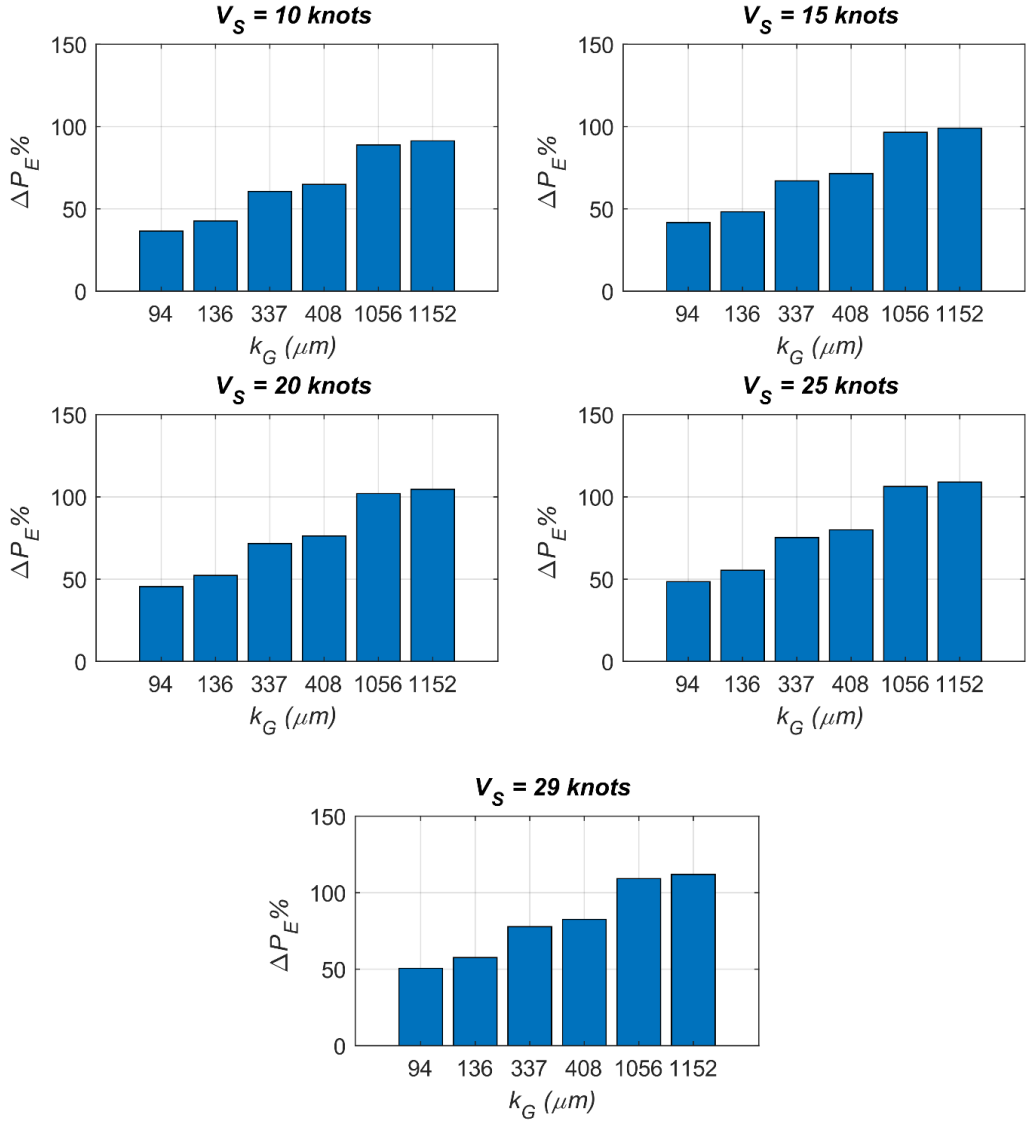

Figure 16 The percentage increases in the P_E due to roughness conditions compared to the smooth condition at five different ship speeds.

As expected, the P_E values rise with an increase in ship speed; however, the rate of this increase is higher at the low speeds compared to the rate at high speeds. This means the effect of roughness is more significant at slow speeds than that of high speeds.

5.5 *The comparison of nominal wakefields for smooth and rough conditions*

The non-dimensional axial velocity distributions were also compared in both smooth and rough cases at 29 knots in Figure 17. It can be seen from the figure that the surface roughness causes a decrease in the flow field at three different locations. The slowing-down effect of wake velocities due to the appendages can also be seen in Figure 17 in comparison with the smooth cases, especially at x/L=0.978.

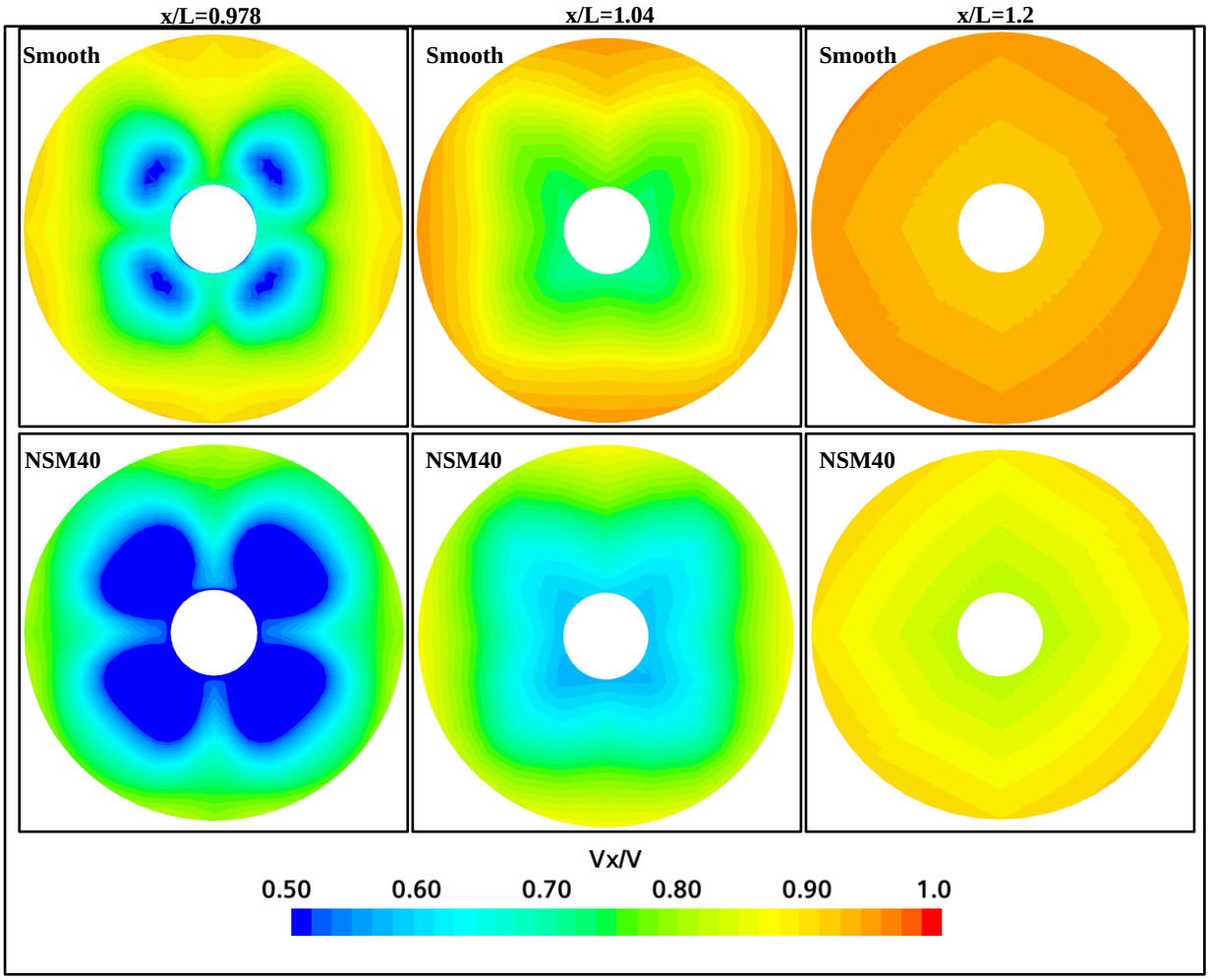

Figure 17 The comparison of non-dimensional axial velocity distributions at 29 knots for smooth and rough conditions.

In order to quantify this effect, the nominal wake fraction was calculated using Equation 19 for the smooth and rough cases. As shown in Table 7, the roughness causes an increase in the nominal wake ranging from 25% to 68% compared to the smooth case. Although the change is still significant, it is not as high as those in C_T, C_{VP} and C_F, under the same surface roughness conditions with increasing *Re* numbers. This can be explained by the fact that the effect of roughness on the nominal wake becomes independent of *Re* number in the fully-rough regime flow condition.

Table 7 Comparison of nominal wake faction for smooth and rough conditions

	Re_S=4.9x10^8	Re_S=7.3x10^8	Re_S=9.8x10^8	Re_S=1.2x10^9	Re_S=1.4x10^9
k_G (μm)	V_S=10 knots	V_S=15 knots	V_S=20 knots	V_S=25 knots	V_S=29 knots
0	0.249	0.242	0.237	0.233	0.231
94	0.312	0.312	0.311	0.311	0.311
136	0.322	0.321	0.321	0.321	0.321
337	0.348	0.348	0.348	0.348	0.348
408	0.354	0.354	0.354	0.354	0.354
1056	0.387	0.386	0.386	0.386	0.386
1152	0.390	0.390	0.389	0.389	0.389

6 FURTHER REMARKS AND CONCLUSIONS

This study shows the applicability of the CFD method in predicting the effect of roughness on the hydrodynamic characteristics of a full-scale submarine. The roughness functions from the literature were employed in the wall functions of CFD software STAR CCM+. The study includes three different steps of simulations. First, model scale simulations were conducted to validate the CFD model with the experimental data. Following that, model and full-scale simulations were conducted in the smooth condition to investigate the scale effect on total resistance components as well as nominal wake distribution. Finally, roughness effects on total resistance and its components as well as nominal wake were investigated and discussed with a view to self-propulsion simulations as the future work.

The differences between the model scale and full-scale simulations are identified and discussed as the scale effect. These differences are due to the Reynolds number dependence of the flow field, which is likely to be ignored in the model scale testing. The ratio of the boundary layer thickness is one of the most important parameters contributing to these differences, which is significantly reduced in full-scale. The comparison of the model and full-scale non-dimensional axial velocities at the propeller plane and its downstream (x/L=0.978, 1.04 and 1.2) indicated that the full-scale values are higher compared to those of the model scale resulting in smaller nominal wake fractions.

The frictional resistance coefficients obtained by the CFD simulations for the full-scale submarine and Granville's similarity law scaling method generally showed a good agreement with each other.

The CFD analysis of the hull pressures indicated that the surface roughness decreases the non-dimensional pressure coefficient, especially at the stern and sail region, which increases the viscous pressure resistance. It is of note that the pressure distributions for the smooth and rough cases are similar on the bow and parallel mid-body section of the hull, which means that the roughness does not affect the pressure distribution unless there is an adverse pressure gradient (e.g. around appendages). The results are consistent with the previous studies in the literature.

It was observed that the total resistance coefficient and hence the effective power of the submarine was further increased with increasing roughness as expected. However, it was interesting to note that, increasing ship speed did not decrease the effect of surface roughness on the total resistance, as reported in Song et al. [26] for a surface ship case. This can be

attributed to the wave-making resistance of the surface ship emerging as the significant contributor to the total resistance coefficient at high speeds while the roughness effect does not diminish with increasing ship speed.

The study showed that increasing roughness height also has detrimental effects on the nominal wake with the increasing wake fraction values from 25% to 68%, which may significantly impact the propeller inflow and hence the advance velocity of the propeller. The increase in wake would increase propeller efficiency.

Furthermore, the change in the propeller inflow due to roughness, will also affect the propeller's cavitation inception, which is critical for any naval vessel, especially for submarines. Therefore, the current study is being further expanded to include the self-propulsion, including the cavitation modelling, to investigate the effect of the roughness on the self-propulsion, cavitation, and ultimately on the underwater radiated noise of submarines.

On a final note, the hull roughness presented in this study is mainly associated with the barnacle type biofouling with different heights and coverage based on which the roughness functions were derived. While this type of macrofouling is quite common, more cautious navies and commercial shipowners may not allow the growth of this macrofouling type by cleaning their vessels more often. However, the physical hull roughness by welding, coatings etc. as well as the most common micro size biofouling, i.e. biofilm (or slime), is unavoidable and should be taken into account at the performance prediction of any vessel, including submarines. Within this context, there is a need for the roughness functions of these surfaces with more realistic or simulated hull roughness (i.e. due to welding, coatings, etc.) including the effect of dynamic biofilm growth. Such data is rather rare, although it has been recently reported in Yeginbayeva et al. [34, 73] for commercial foul release coatings that can be easily simulated with the method presented in this study for more realistic fouling scenarios.

7 ACKNOWLEDGEMENT

The second author is sponsored by the Stone Marine Propulsion Ltd of the UK and the University of Strathclyde during his PhD study. The Turkish Ministry of Education funds Mr Refik Ozyurt`s doctoral study. Results were obtained using the ARCHIE-WeSt High Performance Computer (www.archie-west.ac.uk) based at the University of Strathclyde. This work is partially supported by MarEd (Maritime Education for Energy Efficiency) Project by European Commission under the framework of Erasmus+ KA2 Cooperation for Innovation and the Exchange of Good Practices, KA202 Strategic Partnership for vocational education and training (Grant Number: 2018-1-TR01-KA202-058717)

8 REFERENCES

[1] Bixler GD, Bhushan B. Fluid Drag Reduction with Shark-Skin Riblet Inspired Microstructured Surfaces. Advanced Functional Materials. 2013;23:4507-28.
[2] Froude W. Report to the Lords Commissioners of the Admiralty on Experiments for the Determination of the Frictional Resistance of Water on a Surface Under Various Conditions.: Report of the British Association for the Advancement of Science; 1874.
[3] Froude W. Experiments on the Surface-Friction Experienced by a Plane Moving Through Water.: Report of the British Association for the Advancement of Science; 1872.
[4] Institute WHO. Marine Fouling and its prevention. ANNAPOLIS, MARYLAND: U. S. NAVAL INSTITUTE; 1952.
[5] Izubuchi T. Effect of fouling of ship's bottom on the resistance of ships. Journal of Zosen Kiokai. 1934;1934:57-100.
[6] Davis HFD. The Increase in SHP and RPM due to Fouling. Jour Am Soc Nav Eng. 1930;42:155-66.
[7] Kempf G. A Study of Ship Performance in Smooth and Rough Water. Trans Soc Nav Arch and Mar Eng. 1936;44:195-227.
[8] Liljegren CO. Naval Architecture as Art and Science: Cornell Maritime Press; 1943.
[9] McEntee W. Variation of Frictional Resistance of Ships with Condition of Wetted Surface. Trans Soc Nav Arch and Mar Eng. 1915;23:37-42.
[10] Lewthwaite JC, Molland A, Thomas K. An investigation into the variation of ship skin frictional resistance with fouling. Royal Institution of Naval Architects Transactions. 1985;127.
[11] Haslbeck EG, Bohlander GS. Microbial biofilm effects on drag-lab and field. Naval surface warfare center carderock div annapolis MD; 1992.
[12] Benson J, Ebert J, Beery T. Investigation in the NACA tank of the effect of immersion in salt water on the resistance of plates coated with different shipbottom paints. NACA Memorandum Report C&R C-S19-1 (3). 1938.
[13] Lewkowicz A, Das D. Turbulent boundary layers on rough surfaces with and without a pliable overlayer: a simulation of marine fouling. International shipbuilding progress. 1986;33:174-86.
[14] Watanabe S, Nagamatsu N, Yokoo K, Kawakami Y. The augmentation in frictional resistance due to slime. J Kansai Soc Naval Architects. 1969;131:45-51.
[15] Loeb G, Laster D, Gracik T. The influence of microbial fouling films on hydrodynamic drag of rotating discs. Marine biodeterioration: an interdisciplinary study. 1984:88-94.
[16] Picologlou BF, Zelver N, Characklis WG. Biofilm growth and hydraulic performance. Journal of the Hydraulics Division1980. p. 733-46.
[17] Schultz M. The effect of biofilms on turbulent boundary layers. Florida, US: Florida Institute of Technology; 1998.
[18] Schultz M, Swain G. The effect of biofilms on turbulent boundary layers. J Fluids Eng. 1999;121 (1):44-51.
[19] Turkmen S, Atlar M, Yeginbayeva I, Benson S, Finlay JA, Clare AS. Frictional drag measurements of large-scale plates in an enhanced plane channel flowcell. Biofouling. 2020;36:169-82.
[20] Schultz MP. Frictional Resistance of Antifouling Coating Systems. Journal of Fluids Engineering. 2004;126:1039-47.
[21] Schultz MP. Effects of coating roughness and biofouling on ship resistance and powering. Biofouling. 2007;23:331-41.

[22] Granville PS. Similarity-Law Characterization Methods for Arbitrary Hydrodynamic Roughnesses. DAVID W TAYLOR NAVAL SHIP RESEARCH AND DEVELOPMENT CENTER BETHESDA MD SHIP …; 1978.
[23] Granville PS. The frictional resistance and turbulent boundary layer of rough surfaces. Journal of ship research. 1958;2:52-74.
[24] Demirel YK, Uzun D, Zhang Y, Fang HC, Day AH, Turan O. Effect of barnacle fouling on ship resistance and powering. Biofouling. 2017;33:819-34.
[25] Uzun D, Ozyurt R, Demirel YK, Turan O. Does the barnacle settlement pattern affect ship resistance and powering? Applied Ocean Research. 2020;95.
[26] Song S, Demirel YK, Atlar M. An investigation into the effect of biofouling on the ship hydrodynamic characteristics using CFD. Ocean Engineering. 2019;175:122-37.
[27] Womack K, Schultz M, Meneveau C. Effect of barnacle density on hydrodynamic drag. 19TH INTERNATIONAL CONGRESS ON MARINE CORROSION AND FOULING, Melbourne, Florida2018.
[28] Gowing S, Chang P, Dehn C, Storms S. Measurements of biofouling drag using a 2-D channel flow apparatus with models of bio-fouled panels. 19TH INTERNATIONAL CONGRESS ON MARINE CORROSION AND FOULING, Melbourne, Florida2018.
[29] Grigson C. Drag losses of new ships caused by hull finish. Journal of Ship Research. 1992;36:182-96.
[30] Schultz MP, Myers A. Comparison of three roughness function determination methods. Experiments in Fluids. 2003;35:372-9.
[31] Clauser FH. Turbulent Boundary Layers in Adverse Pressure Gradients. Journal of the Aeronautical Sciences. 1954;21:91-108.
[32] Nikuradse J. Stromungsgesetz in rauhren rohren, vDI Forschungshefte 361 (English translation: Laws of flow in rough pipes). Tech Rep NACA Technical Memorandum 1292. Washington, DC, USA (1950): National Advisory Commission for Aeronautics; 1933.
[33] Granville PS. Drag-characterization method for arbitrarilyrough surfaces by means of rotating disks. Journal of Fluids Eng 1982;104:373-7.
[34] Yeginbayeva IA, Granhag L, Chernoray V. Review and historical overview of experimental facilities used in hull coating hydrodynamic tests. Proceedings of the Institution of Mechanical Engineers, Part M: Journal of Engineering for the Maritime Environment. 2018;233:1240-59.
[35] Schultz MP. The Relationship Between Frictional Resistance and Roughness for Surfaces Smoothed by Sanding. Journal of Fluids Engineering. 2002;124:492-9.
[36] Flack KA, Schultz MP. Review of hydraulic roughness scales in the fully rough regime. Journal of Fluids Engineering. 2010;132.
[37] Uzun D, Demirel YK, Coraddu A, Turan O. Time-dependent biofouling growth model for predicting the effects of biofouling on ship resistance and powering. Ocean Engineering. 2019;191.
[38] Eça L, Hoekstra M. Numerical aspects of including wall roughness effects in the SST k–ω eddy-viscosity turbulence model. Computers & Fluids. 2011;40:299-314.
[39] Lin T, Bywater R. Turbulence models for high-speed, rough-wall boundary layers. AIAA Journal. 1982;20:325-33.
[40] Christoph GH, Pletcher RH. Prediction of rough-wall skin friction and heat transfer. AIAA Journal. 1983;21:509-15.
[41] Lakehal D. Computation of turbulent shear flows over rough-walled circular cylinders. Journal of Wind Engineering and Industrial Aerodynamics. 1999;80:47-68.
[42] Gre´goire G, Favre-Marinet M, Amand FJS. Modeling of Turbulent Fluid Flow Over a Rough Wall With or Without Suction. Journal of Fluids Engineering. 2003;125:636-42.

[43] Saeed F. Numerical Models For Boundary-Layer Analysis On Rough Surfaces. ARA Journal. 2004;2003:180-5.
[44] Louda P, PrÌŒÃ-hoda Jr, Kozel K. Numerical modelling of turbulent flow over rough walls. Pamm. 2007;7:4100011-2.
[45] Apsley D. CFD Calculation of Turbulent Flow with Arbitrary Wall Roughness. Flow, Turbulence and Combustion. 2007;78:153-75.
[46] Khor YS, Xiao Q. CFD simulations of the effects of fouling and antifouling. Ocean Engineering. 2011;38:1065-79.
[47] Castro AM, Carrica PM, Stern F. Full scale self-propulsion computations using discretized propeller for the KRISO container ship KCS. Computers & Fluids. 2011;51:35-47.
[48] Demirel YK, Khorasanchi M, Turan O, Incecik A, Schultz MP. A CFD model for the frictional resistance prediction of antifouling coatings. Ocean Engineering. 2014;89:21-31.
[49] Demirel YK, Turan O, Incecik A. Predicting the effect of biofouling on ship resistance using CFD. Applied Ocean Research. 2017;62:100-18.
[50] Schultz MP, Flack KA. The rough-wall turbulent boundary layer from the hydraulically smooth to the fully rough regime. Journal of Fluid Mechanics. 2007;580:381-405.
[51] Farkas A, Degiuli N, Martić I. Towards the prediction of the effect of biofilm on the ship resistance using CFD. Ocean Engineering. 2018;167:169-86.
[52] Farkas A, Degiuli N, Martić I. Impact of biofilm on the resistance characteristics and nominal wake. Proceedings of the Institution of Mechanical Engineers, Part M: Journal of Engineering for the Maritime Environment. 2019;234:59-75.
[53] Speranza N, Kidd B, Schultz MP, Viola IM. Modelling of hull roughness. Ocean Engineering. 2019;174:31-42.
[54] Andersson J, Oliveira DR, Yeginbayeva I, Leer-Andersen M, Bensow RE. Review and comparison of methods to model ship hull roughness. Applied Ocean Research. 2020;99.
[55] Song S, Demirel YK, Atlar M, Shi W. Prediction of the fouling penalty on the tidal turbine performance and development of its mitigation measures. Applied Energy. 2020;276:115498.
[56] Putnam D. OHIO Class External Hull Antifouling. 2016.
[57] Vaz G, Toxopeus S, Holmes S. Calculation of manoeuvring forces on submarines using two viscous-flow solvers. International Conference on Offshore Mechanics and Arctic Engineering2010. p. 621-33.
[58] Chase N. Simulations of the DARPA Suboff submarine including self-propulsion with the E1619 propeller: University of Iowa; 2012.
[59] Chase N, Carrica PM. Submarine propeller computations and application to self-propulsion of DARPA Suboff. Ocean Engineering. 2013;60:68-80.
[60] Sezen S, Dogrul A, Delen C, Bal S. Investigation of self-propulsion of DARPA Suboff by RANS method. Ocean Engineering. 2018;150:258-71.
[61] Schultz MP, Swain GW. The influence of biofilms on skin friction drag. Biofouling. 2000;15:129-39.
[62] Ioselevich V, Pilipenko V. Logarithmic velocity profile for flow of a weak polymer solution near a rough surface. SPhD. 1974;18:790.
[63] Groves NC, Huang TT, Chang MS, David Taylor Research C. Geometric characteristics of DARPA suboff models : (DTRC model nos. 5470 and 5471). Bethesda, MD: David Taylor Research Center; 1989.
[64] ITTC. Recommended Procedures and Guideline Practical Guidelines for Ship CFD Applications, 2011-7.5-0.3, ITTC. 2011.
[65] Date JC, Turnock SR. A study into the techniques needed to accurately predict skin friction using RANS solvers with validation against Froude's historical flat plate experimental data. 1999.

[66] Roache PJ. QUANTIFICATION OF UNCERTAINTY IN COMPUTATIONAL FLUID DYNAMICS. Annual Review of Fluid Mechanics. 1997;29:123-60.
[67] Procedure for Estimation and Reporting of Uncertainty Due to Discretization in CFD Applications. Journal of Fluids Engineering. 2008;130.
[68] Roache PJ. Verification of Codes and Calculations. AIAA Journal. 1998;36:696-702.
[69] Stern F, Wilson R, Shao J. Quantitative V&V of CFD simulations and certification of CFD codes. International journal for numerical methods in fluids. 2006;50:1335-55.
[70] Carlton JS. Marine Propellers and Propulsion. 4th Edition ed2018.
[71] Atlar M. Hydrodynamics, Resistance & Propulsion Lecture Notes. University of Strathclyde; 2020.
[72] Wang Z-Z, Xiong Y, Wang R, Shen X-R, Zhong C-H. Numerical study on scale effect of nominal wake of single screw ship. Ocean Engineering. 2015;104:437-51.
[73] Yeginbayeva IA, Atlar M. An experimental investigation into the surface and hydrodynamic characteristics of marine coatings with mimicked hull roughness ranges. Biofouling. 2018;34:1001-19.